

Label-free chip-based evanescent light scattering super-resolution and superior-contrast optical microscopy (cELS)

NIKHIL JAYAKUMAR,^{1,6} FIREHUN T DULLO,² VISHESH DUBEY,¹ AZEEM AHMAD,¹ JENNIFER CAUZZO,³ EDUARDA MAZAGAO GUERREIRO,⁴ OMRI SNIR,⁴ NATASA SKALKO-BASNET,³ KRISHNA AGARWAL,¹ AND BALPREET SINGH AHLUWALIA^{1,5,7}

¹ Department of Physics and Technology, UiT The Arctic University of Norway, Tromsø 9037, Norway

² SINTEF Digital, Department of Microsystems and Nanotechnology, Gaustadalleen 23C, 0373 Oslo, Norway

³ Department of Pharmacy, Faculty of Health Sciences, UiT The Arctic University of Norway, Tromsø 9037, Norway

⁴ Department of Clinical Medicine, UiT The Arctic University of Norway, Tromsø 9037, Norway

⁵ Department of Clinical Science, Intervention and Technology, Karolinska Institute, 17177 Stockholm, Sweden

⁶nik.jay.hil@gmail.com, ⁷balpreet.singh.ahluwalia@uit.no

Abstract: Chip-based Evanescent Light Scattering (cELS) utilizes the multiple modes of a high-index contrast optical waveguide for near-field illumination of unlabeled samples, thereby repositioning the highest spatial frequencies of the sample into the far-field. The multiple modes scattering off the sample with different phase differences is engineered to have random spatial distributions within the integration time of the camera, mitigating the coherent speckle noise. This enables label-free superior-contrast imaging of weakly scattering nanosized specimens such as extra-cellular vesicles (EVs) and liposomes, dynamics of living HeLa cells etc. The article explains and validates experimentally the physics behind cELS by demonstrating a multi-moded straight waveguide as a partially coherent light source. For isotropic super-resolution, spatially incoherent light engineered via multiple-arms waveguide chip and intensity-fluctuation based algorithms are used. The proof-of-concept results are demonstrated on 100 nm polystyrene beads and resolution improvement of close to 2 \times is shown. cELS also realizes (2-10) \times more contrast as opposed to conventional imaging techniques. In addition, cELS platform is miniaturized and enables large field-of-view imaging compared to state-of-the-art label-free techniques. cELS holds a potential for label-free super-resolution imaging of nanosized biological specimens at high-throughput.

© 2020 Optical Society of America under the terms of the [OSA Open Access Publishing Agreement](#)

1. Introduction

The major challenges associated with label-free microscopy of weakly scattering biological specimens are poor contrast and techniques to circumvent the diffraction-limit in the far-field. Diffraction-limited resolution arises due to the inability to capture the high spatial frequencies of the specimen in the far-field, whereas, poor contrast in the optical regime is attributed to a very weak scattered signal in comparison to the illuminating light. Moreover, illuminating these samples with a highly coherent light source like a laser can lead to speckle formation, degrading the image quality even further. Here, we describe the physics of how manipulating the coherence of light in multi-moded waveguides mitigates the abovementioned challenges of poor contrast, speckle noise and diffraction-limited resolution.

Numerous label-free approaches already exist that circumvent the diffraction-limit [1-9]. However, these techniques involve fabrication challenges, are point-scanning and/or near-field methods making it slow and cumbersome especially for biological studies. The diffraction-limited resolution may also be improved via evanescent wave illumination and

post-processing via reconstruction algorithms [10]. A typical way of generating an evanescent wave illumination is using a total internal reflection fluorescence (TIRF) objective. Rotating Coherent Scattering microscopy (ROCS) [11-13] uses evanescent field generated by a diode laser passed through a rotating diffuser to illuminate the sample from all azimuthal directions, in conventional TIR mode. However, a high magnification/N.A. (numerical aperture) TIR objective lens (e.g. 60-100X >1.33 N.A.) is typically used in ROCS, thus limiting the field-of-view (FoV) to small areas such as about 100 x 100 μm^2 . Another elegant way to generate the evanescent field and over much larger areas is via an optical waveguide, i.e. a photonic-chip [14-21]. In this work, we propose using a high-index contrast ($\Delta n \approx 0.5$) multi-moded optical waveguide platform to perform both label-free superior contrast and super-resolution imaging. Our approach based on photonic-chip offers several advantages as outlined below:

1. Only scattered field off the sample reaches the camera and the need for a physical aperture to stop the unscattered light is inherently circumvented, see Fig. 1. Hence, the issue of poor contrast is mitigated without reducing the effective passband of the microscope as in conventional dark-field microscopes.
2. The use of high refractive index waveguide material ($n \approx 2$) enables accessing higher spatial frequencies of the sample [22], see Fig. 2(b), that are typically inaccessible using conventional free-space bulk optics approach or using index-matched waveguide geometries [18]. The high index core, $n_{\text{eff}} = 2$, reduces the speckle size that can be formed to about $2\pi/(k_e + k_{\text{out}})$, where $k_e = 2\pi \cdot n_{\text{eff}} / \lambda_{\text{vac}}$, $k_{\text{out}} = 2\pi \cdot \text{N.A.} / \lambda_{\text{vac}}$, n_{eff} is the effective index of mode, k_e is the magnitude of the incident evanescent wave vector, k_{out} defines the pass-band of the microscope and λ_{vac} is the vacuum wavelength [23].
3. Here the use of coherent light source like laser helps focus very high-power into thin waveguide geometries. The lack of specificity in label-free imaging and consequently multiple scattering issues is partially circumvented by the evanescent field excitation of the low-loss high refractive index material thin (150 nm) waveguides, see Fig. 2(c). This provides excellent optical sectioning to about less than 100 nm and high field intensity [24] which is important for imaging nano-sized weakly scattering objects.
4. Decoupling of excitation and collection light paths generate images over much larger FoV. User-defined imaging objective lens can be used providing scalable magnification (4-100X) without influencing the illumination light path, a feature that is not possible with conventional TIRF-lens approach, see Fig. 1.

Here, we demonstrate experimentally and theoretically the limited angular diversity between the modes of a straight waveguide. The multiple modes are excited within the integration time of the camera to induce different phase delays between the scattered light off the sample to constitute a random walk. This helps mitigate the speckle noise, enhance the contrast, and also achieve super-resolution when used along with intensity-fluctuation based algorithms as recently demonstrated in fluorescence microscopy [25]. For label-free super-resolution imaging, we utilize the scattering of the modes by the sample when illuminated azimuthally from four directions, i.e., spatially incoherent illumination, via multiple-arm optical waveguide along with intensity-fluctuation based algorithms, MUSICAL [26]. Also, the near-field excitation using waveguides is devoid of out-of-focus light which typically hinders the performance of these reconstruction algorithms [27], more so in the label-free mode. Therefore, through this article we put forward the concept of cELS as an attractive non-invasive label-free superior-contrast and super-resolution microscopy technique which can be utilized with intensity-fluctuation based algorithms to circumvent the diffraction-limit. The theory and experimental results presented in this

article substantiate this proposal. See supplementary section S1-S3 and Fig. S(1)-S(4) for additional information about cELS and waveguides in general.

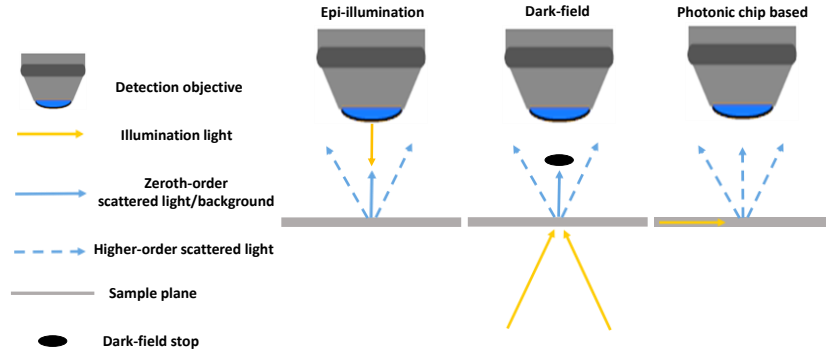


Fig. 1. Comparison between epi-illumination, dark-field and photonic-chip based illumination. Photonic-chip helps decouple the illumination and detection paths and caters to scalable field-of-view. The incident light is given in yellow and scattered light in blue.

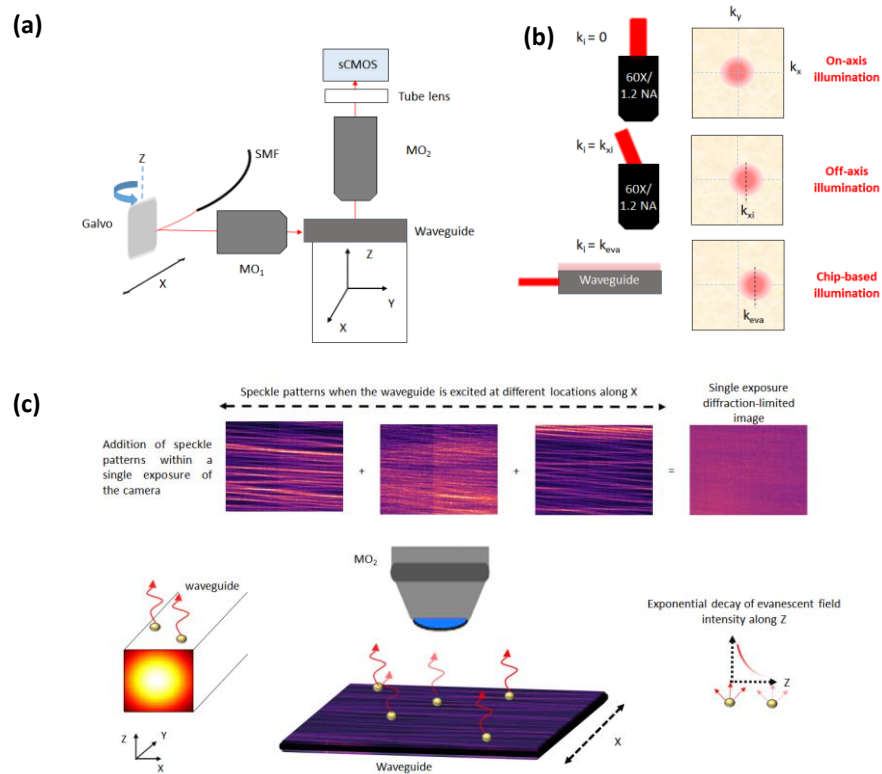


Fig. 2. (a) Schematic of cELS experimental setup. (b) Influence of obliquity of illumination in Fourier domain ($k_x - k_y$ domain). Three different cases corresponding to on-axis epi-illumination ($k_i = 0$), off-axis epi-illumination ($k_i = k_{xi}$) and waveguide chip-based illumination ($k_i = k_{eva}$) and the corresponding object spectrum (shown in off-white texture) they sample are shown. Illumination provided by high-refractive index chip provide access to the higher spatial frequency. (c) Schematic representation of an optical waveguide supporting several guided modes and a few scattering objects that convert the evanescent waves into scattering waves. The addition of speckle patterns at the camera plane helps suppress the speckle noise. A waveguide transmitting power via a fundamental mode of the structure is also shown alongside.

2. Optical setup and imaging conditions

The schematic of cELS experimental setup and its basic principle of working is shown in Fig. 2. The coherent laser (Cobolt Flamenco 660) light, $\lambda_{vac} = 660\text{ nm}$, is coupled into a single mode fiber that delivers collimated light via a collimator onto a galvo mirror which is free to rotate along the z-axis. The galvo helps steer this light onto the back focal plane of a microscope objective (Olympus LMPanFL N 50X/0.5 NA), MO₁. MO₁ focuses the incident collimated light onto the input facet of a waveguide. This configuration enables scanning the incident light on the input facet of the waveguide, exciting different sets of guided mode for each incident location. The waveguide is mounted on a high-precision piezo electric XYZ-translation stage. The sample to be imaged is placed on top of the waveguide core. The evanescent light that interacts with the sample, gets scattered and is collected by a microscope objective MO₂. Via a 4f setup, the scattered light is imaged onto a sCMOS camera (Hamamatsu C13440-20CU). The exposure time of the camera for the different experiments presented in this article is typically about 30 ms. The galvo oscillation rate is set at 1013 Hz for the waveguide widths used in this experiment, a prime number, which causes a spatial re-distribution of the excited modes within the exposure time of the camera. Throughout this article, experiments have been carried out using a silicon nitride (Si₃N₄) waveguide. The fabrication of Si₃N₄ waveguide and the preparation, characterization, and labeling strategies of liposomes, EV's and cells are given in section S4-S6 of the supplementary material.

3. Theory of cELS

The theory section provided here and in the supplementary material focuses on mainly three concepts: (1) collection of near-field information in the far-field, (2) cELS enabling high-contrast imaging and (3) cELS along with intensity-fluctuation based algorithms enable circumventing the diffraction-limit.

3.1 Near-field information to far-field

Optical waveguides arrest the diffractive spreading of light and help transfer power via the modes of the structure. The modes correspond to eigen solutions of Maxwell's equations (MWEQ) for the guiding structure. The boundary conditions imposed by MWEQ at the core-cladding interface of the waveguide mandate the setting up of evanescently decaying fields. As a result, the transfer of optical power in the core along the length of the waveguide is accompanied with the generation of the evanescent wave at the core-cladding interface. However, the evanescent fields do not carry any net energy away from the interface. It means that if an ideal waveguide without any sample is imaged, no light will reach the camera plane. However, any perturbation in index at the core-cladding interface can scatter photons into the camera [28].

The physical mechanism behind the conversion of non-propagating evanescent waves into propagating waves may be understood from the following simplified illustration [23, 29]. A two-dimensional sample is illuminated by an incident field $E(x, y, z)$. Let us represent the two-dimensional Fourier transform of this field by $\tilde{E}(\alpha, \beta; z)$ where α, β and γ are spatial frequencies with respect to x, y and z axis respectively, i.e., propagation vector $\vec{k} = \alpha\hat{x} + \beta\hat{y} + \gamma\hat{z}$. The magnitude of the wave vector of a waveguide mode is $\frac{2\pi}{\lambda_{vac}}n_{eff}$, where n_{eff} is the effective mode index. The evanescent wave vector corresponds to largest spatial frequency components of the field. This field interacts with a thin sample placed at $z = 0$. The sample may be represented by a transmission function $T(x, y)$. Invoking the Born approximation, just after the thin sample the field becomes [23]

$$E_{sample}(x, y; 0) = T(x, y)E(x, y; 0) \quad (1)$$

By the property of Fourier transform, Eq. (3) may be represented alternatively as the convolution of the two signals in spatial frequency domain as

$$\tilde{E}_{sample}(\alpha', \beta'; 0) = \iint_{-\infty}^{\infty} \tilde{E}(\alpha, \beta; 0) \hat{T}(\alpha - \alpha', \beta - \beta') d\alpha d\beta \quad (2)$$

But the illuminating field may be represented via the sifting property of delta function as follows

$$\tilde{E}(\alpha, \beta; 0) = \iint_{-\infty}^{\infty} \tilde{E}(\tilde{\alpha}, \tilde{\beta}; 0) \delta(\tilde{\alpha} - \alpha, \tilde{\beta} - \beta) d\tilde{\alpha} d\tilde{\beta} \quad (3)$$

Combining Eq. (2) and (3) it can be seen that the spatial frequencies of the sample represented by $\hat{T}(\alpha, \beta)$ gets convolved with the spatial frequencies of the incident field. Or in other words, if a mode of an evanescent field is represented by $\delta(\alpha_{eva}, \beta_{eva})$, then the electric field just after the thin sample contains the shifted object spectrum $\hat{T}(\alpha - \alpha_{eva}, \beta - \beta_{eva})$, where α_{eva} and β_{eva} are the spatial frequencies of the evanescent wave illuminating the sample. If the shifted version of the function falls within the passband of the microscope, those high spatial frequencies of the object will reach the camera plane. Thus, sub-diffraction limit sized features or high spatial frequencies is captured using cELS due to high n_{eff} of the waveguide core that is typically not accessible with conventional objective based illumination schemes. This is illustrated in Fig. 2(b).

3.2 cELS enables superior contrast imaging

In conventional bright field imaging, the incident light $E_i(\mathbf{r}, t)$ and the light scattered off the sample $E_s(\mathbf{r}, t)$ reaches the camera as shown in Fig. 1. The total complex scalar field at the camera plane is $E_T(\mathbf{r}, t) = E_i(\mathbf{r}, t) + E_s(\mathbf{r}, t)$. For weakly scattering specimens, the only modulation in total field will be in its phase. But the camera is not sensitive to this phase information, i.e., the intensity recorded by the camera will $\langle I(\mathbf{r}, t) \rangle$ has no phase information, where $\langle \rangle$ represents time averaging. It implies that there is little modulation in intensity, and therefore almost no contrast. But while imaging using waveguides such as in cELS, the incident light does not reach the camera but only the scattered light off the sample gets detected, i.e., $E_T(\mathbf{r}, t) = E_s(\mathbf{r}, t)$ and therefore, the point will be visible with enhanced contrast as a bright spot on a dark background.

Let us consider two point scatterers represented by $j=1,2$. The incident field induces Rayleigh dipoles [30] which radiate into the far-field. Let the field emitted by each emitter at the camera plane be given by $E_j(\mathbf{r}, t) = E_0(\mathbf{r}) \exp[i\varphi_j(\mathbf{r}, t) - i\omega t]$. Here we assume that the scatterers have the same amplitude of the dipoles, resulting in the same field amplitude individually. The total field intensity averaged over the integration time of the camera is then represented as [31]

$$\langle I(\mathbf{r}, t) \rangle = 2|E_0(\mathbf{r})|^2 + 2|E_0(\mathbf{r})|^2 \langle \cos(\chi(\mathbf{r}, t)) \rangle \quad (4A)$$

where

$$\chi(\mathbf{r}, t) = \varphi_1(\mathbf{r}, t) - \varphi_2(\mathbf{r}, t) \quad (4B)$$

First, let us consider a situation of coherent illumination. Although the phases $\varphi_1(\mathbf{r}, t)$ and $\varphi_2(\mathbf{r}, t)$ are a function of time, the phase difference $\chi(\mathbf{r}, t)$ is time-invariant and can be simply represented as $\chi(\mathbf{r})$. The cosine term in Eqn. (4A) also becomes time invariant and therefore, the interference phenomenon is clearly witnessed in the images. In the case of incoherent illumination, the phase difference $\chi(\mathbf{r}, t)$ is not time-invariant and the cosine term is a function of temporal variations. Since the phase fluctuations occur on a time scale much smaller than the integration time of the camera, the time averaged cosine term tends to zero and therefore no interference is observed.

However, multi-moded illumination patterns inside the photonic waveguides presents a very interesting case. Let the electric fields emitted from the scatterers due to a particular mode m be represented as $E_{j,m}(\mathbf{r}, t) = E_{0,m}(\mathbf{r}) \exp[i\varphi_{j,m}(\mathbf{r}, t) - i\omega_m t]$, where the subscript m denotes the mode. Correspondingly, the subscript m may be introduced in $I_m(\mathbf{r}, t)$ and $\chi_m(\mathbf{r})$ as well. Since the modes are coherent individually and with respect to each other, the time term in the function $\chi_m(\mathbf{r}, t)$ is absent. At any given point of time t ,

due to galvo scanning, the mode combination is different. Representing the complex mode coefficients at a given time t as $a_m(t)$, the average intensity within an integration time due to all the mode combinations is given as

$$\langle I(\mathbf{r}, t) \rangle = \left\langle 2|a_m(t)|^2 |E_{0,m}(\mathbf{r})|^2 + 2|a_m(t)|^2 |E_{0,m}(\mathbf{r})|^2 \cos(\chi_m(\mathbf{r}) - \alpha_m(t)) \right\rangle \quad (5)$$

where $\alpha_m(t)$ represents the phase of $a_m(t)$. The presence of a time varying cosine term $\cos(\alpha_m(t))$ which changes continuously with the galvo scan position implies that the average intensity shown in Eq. (5) is no longer coherent. However, it is also not strictly incoherent because the galvo scan times are comparable to the camera exposure time. In order to ensure that there is no strict correlation between the images acquired across different frames we use a galvo scan rate of a prime number. In essence, we realize a partially coherent illumination case per frame. However, if we were to consider an infinite acquisition time, or several frames under this set-up, it would result into a close to ideal incoherence situation. Eqn. (5) may also be understood as a large number of speckle patterns getting added at the camera plane, mimicking a random walk. The central limit theorem suggests that the contrast of these speckles scale as $1/\sqrt{N}$ when added on an intensity basis, where N is the number of independent speckle patterns added [32]. Thus, the issue of coherent noise is mitigated via the usage of a multi-moded waveguide and galvo scanning, demonstrating a multi-moded waveguide as a partially coherent light source that enables high-contrast imaging.

3.3 cELS supports super-resolution imaging

To understand how cELS when used in tandem with intensity-fluctuation based algorithms helps circumvent the diffraction-limit, the following scenario is presented. Assume two scatterers separated by Rayleigh distance = $0.61\lambda/\text{NA}$, where NA is the numerical aperture of the microscope objective and λ is the wavelength of detected light. In the case of incoherent imaging, i.e., if the scatterers are replaced by fluorescent molecules, they will be resolved as per Rayleigh's resolution criteria. However, in case of cELS, in addition to fluctuations due to multi-moded illumination pattern, the role of interference between the scatterers present an interesting scenario. The details of two scatters illuminated by a waveguide chip are discussed in supplementary section S2. Excitation of two scatters in label-free mode by waveguide chip has two aspects opposite to one another in terms of analogy with the fluorescence particles, as listed below.

1. The same mode of the waveguide excites both the scatterers. The phase difference between the light scattered off the scatterers can be shown to be approximately 1.6 radians, rigorous analysis is presented in supplementary section S2. It implies that the resolvability of the two scatterers at the camera plane is more challenging than the resolvability of two fluorescent particles.
2. Two different modes of the waveguide excite the scatterers. The phase difference between the light scattered off the scatterers can then be shown to be π radians, as detailed in supplementary section S2. This intensity distribution at the camera plane is similar to what is observed as in the case of incoherent illumination.

As the galvo oscillates to vary the illumination patterns in the waveguide, the complex mode coefficient $a_m(t)$ changes with time, i.e., both the amplitude and phase of the scattered light changes. An image stack so acquired over time exhibits fluctuations in intensity due to this multi-moded illumination pattern. However, this is in contrast to fluorescence microscopy where the fluorescent molecules, typically a few nanometers in

size, emit independently and portrays a linear mapping between the fluorophore concentration and image plane. But the partial coherent imaging nature of cELS may lead to artifacts due to interference between scattered light off the scatterers, i.e., the sample plane concentration and image plane intensity obey a non-linear relation. Thus, albeit at the cost of some reconstruction artifacts cELS provides a technique to circumvent the diffraction-limit in label-free mode.

4. Proof-of-concept results and discussion

The results presented here are categorized into three parts: (a) 60 nm polystyrene nanobeads, (b) weakly scattering nanosized biological specimens like liposomes and extracellular vesicles, (c) biological cells (d) and super-resolved label-free imaging of 100 nm polystyrene nanobeads. The dynamics of live HeLa cells is attached as a supplementary movie. Details of experimental parameters are provided in supplementary material Table 1.

4.1 Weakly scattering specimens

Firstly, 60nm polystyrene nanobeads are imaged to compare the TIRF and cELS performance. Fig. 3(a) shows the images of 60 nm polystyrene beads acquired in cELS and TIRF mode and the two images are in good agreement. The signal to background ratio (SBR) is higher for cELS as shown. The Fourier transform of the TIRF image shows that higher spatial frequencies get attenuated faster which is the case for incoherent imaging. On the other hand, cELS is a partially coherent imaging technique and therefore, the contrast does not drop significantly even for the higher spatial frequencies which is expected for coherent imaging. Thus, cELS supports superior contrast imaging of nanosized structures that corresponds to higher spatial frequencies. The difference in Fourier spectrum between the coherent and incoherent imaging is further discussed in supplementary material.

Next, we opted for samples that are both weakly scattering and are nanoscale in size, liposomes. The index contrast of liposome with its surrounding is only about 0.04 [33] and the size of the liposomes used here is about 125 nm. This constitutes a weakly scattering specimen. To detect these structures, they are prepared including fluorescent molecules. But due to their limited size, the fluorescence signal emitted by the structures are usually weak as also shown in our studies. cELS helps image these structures with high contrast and therefore, when combined with image segmentation algorithms can be used for estimating the particle density. Thanks to the use of high-refractive index contrast of the waveguide material, together with a thin waveguide geometry (150 nm thick), the evanescent field intensity at the waveguide surface is high and decay rapidly, aiding to generate label-free images with higher signal to background noise as opposed to the TIRF. Further, cELS image shows the presence of larger number of particles whereas TIRF image of the same region of interest showed fewer number of particles, see also Fig. S5 of supplementary material. This could be attributed to bleaching out of the fluorescence or due to faint a fluorescence signal. A similar behavior is also noted in Ref. [20].

In Fig. 3(b)-3(e), we compare the imaging of liposomes using different light sources and different geometries. Here, laser and pseudo-thermal light sources (PTS) are used both in the epi-illumination mode; and TIRF and cELS in the near-field illumination mode via the photonic-chip. A PTS is a spatially incoherent light source generated by passing laser through a rotating diffuser to reduce the coherent noise [32]. As anticipated, the laser in the epi-fluorescence mode generates coherent noise that hinders coherent label-free imaging of weakly scattering nano-object, Fig. 3(b). The coherent noise however can be reduced using dynamic speckle-illumination (DSI) of PTS. Nevertheless, even after addressing the coherent noise issue, the epi-configuration mode containing the unscattered light generates comparable background noise as compared to that of a weakly scattering object, consequently reducing the contrast of the images. By exploiting fluorescence tagging and near-field excitation such as in conventional TIRF helps reduce of the out-of-focus light and can improve the image contrast. However, this method still suffers from photo-bleaching, labelling non-uniformity, background fluorescence signals from unspecific labelling that are inherent to fluorescence-based approaches. Contrary to all

these approaches, cELS generates superior contrast imaging of liposome in label-free mode which is devoid of bleaching issues as well as explored next.

Fig. 3(f) shows the time-lapse imaging of another weakly scattering object, <225 nm extra-cellular vesicles (EVs). Photo-bleaching is a well-known problem in fluorescence microscopy and the bleaching of the fluorescence signal from the EVs is illustrated via the TIRF images. It can be seen that the fluorescence molecules bleached out over time in TIRF mode whereas cELS continued to show their presence even after photo-bleaching. This illustrates the time-lapse label-free imaging capability of cELS that would find application for imaging of nano-sized biological structures like liposomes or EVs where the fluorescence signal will be limited.

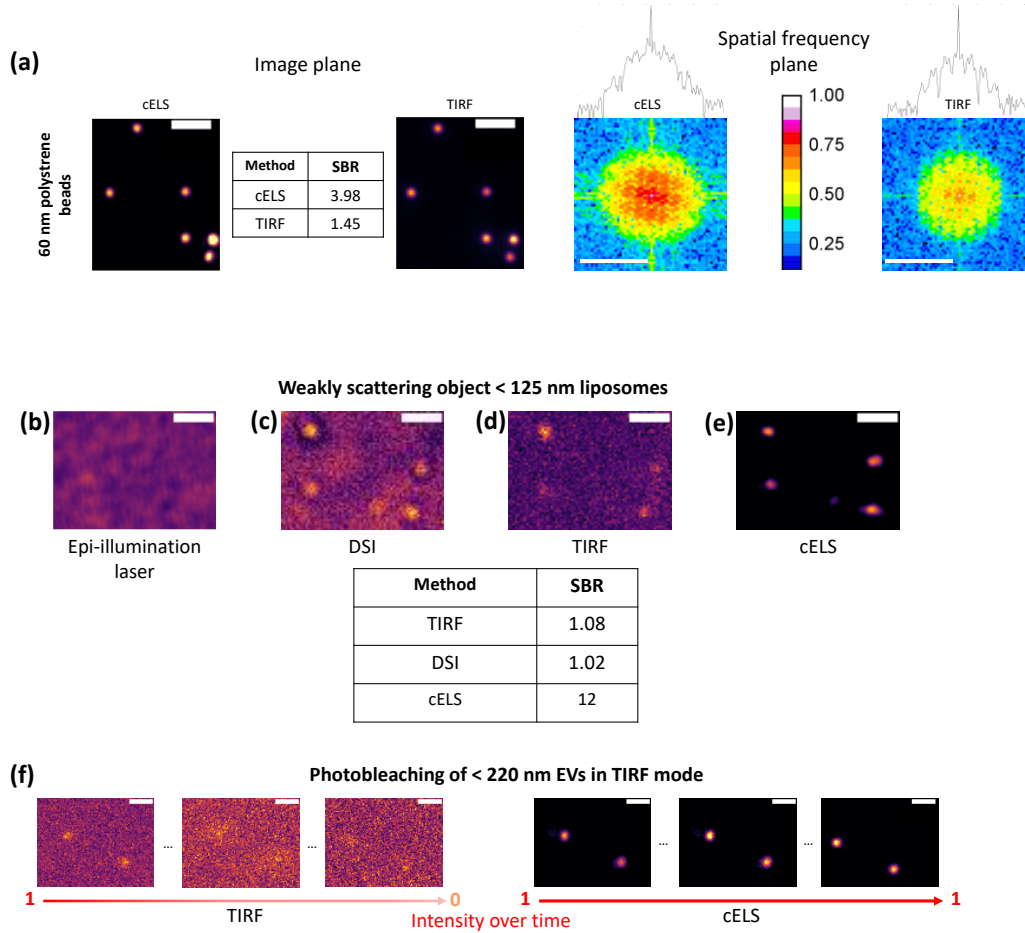


Fig. 3. (a) cELS and TIRF images of 60 nm polystyrene beads. The signal to background ratio (SBR) is given in the table and the Fourier transform of the beads imaged using cELS and TIRF is given alongside. Scale bar 2 μ m in the image plane and 5 μ m $^{-1}$ in the spatial frequency plane. (b) Liposomes of < 125 nm in size imaged using epi-illumination laser mode, (c) TIRF mode, (d) DSI mode and (e) cELS are compared. The corresponding SBR is given in the table below. Scale bar 2 μ m. (f) cELS and TIRF images of < 225 nm sized extracellular vesicles (EVs). The TIRF image shows photo-bleaching with time whereas cELS allows long-term imaging of the EVs. Scale bar 2 μ m.

Fig. 4 showcases the capability of cELS to support superior-contrast imaging for scalable FoV offered by different imaging objective lens. Here, 100 nm polystyrene beads are imaged in cELS, epi-illumination mode both with DSI and white light (WL) sources using two different objectives lenses 20X/0.45N.A. The isolated nano-beads are not visible with both DSI and WL. Only the aggregated 100 nm beads are barely visible with DSI and white light sources. Contrary, cELS approach provide high-contrast images irrespective of the low or high magnification objective lens, thus providing superior contrast imaging over

large FoV region supported by low magnification objective lens. This is attributed to a multitude of factors like decoupled coherent illumination/detection in dark-field mode and use of high refractive index waveguide material. The high effective index of the guided modes scatters the dominant high spatial frequency components of the nano-sized sample. The coherent nature of the scattered light, which contains the dominant high spatial frequencies of the sample, aids in interference at the image plane to generate contrast. On the other hand, in epi-illumination mode the illumination and detection schemes are coupled and both the light sources, i.e. spatially incoherent light (partially incoherent) for DSI and temporally incoherent light for WL fails to generate sufficient contrast. Thus, cELS support superior-contrast imaging of weakly scattering object also for low magnification lens, that benefit from imaging over large FoV, see supplementary Fig. S6.

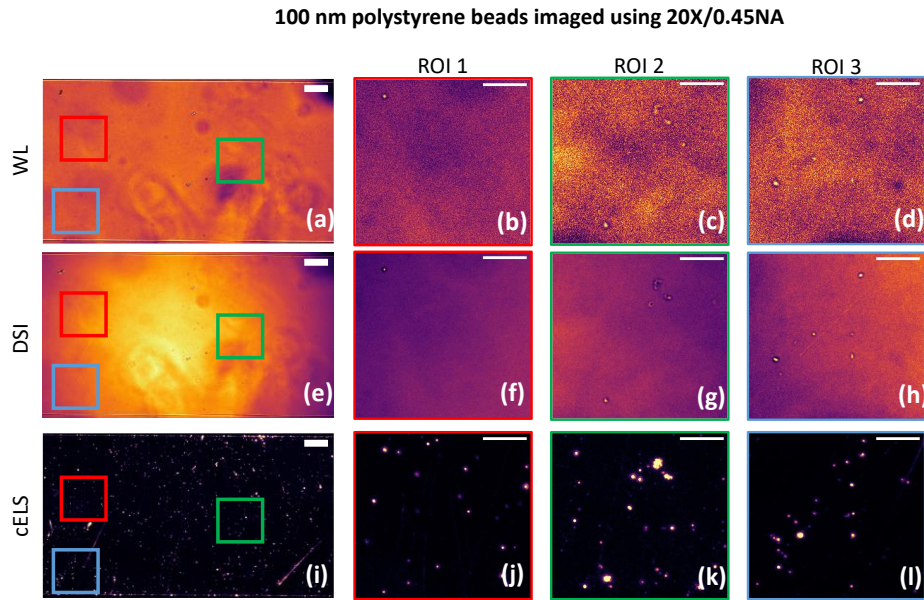


Fig. 4. 100 nm polystyrene beads imaged using 20X/0.45NA with white light (WL), dynamic speckle illumination (DSI) and cELS. (a,e,i) 100 nm beads imaged using WL, DSI and cELS respectively. Scale bar 50 μ m. A few regions of interest, ROI 1-3, with aggregated and sparse beads are chosen within the FoV enclosed by red, green and blue boxes which are blown up and displayed. (b,c,d) WL images of 100 nm beads, (f,g,h) 100 nm beads imaged in DSI mode and (j,k,l) 100 nm beads imaged using cELS. Scale bar 20 μ m in the blown-up regions.

4.2 cELS for imaging cells

Fig. 5 compares cELS and TIRF image of a fixed HeLa cell. cELS imaging was performed at 660 nm excitation and detection. For TIRF imaging, the actin filaments were labeled at 532 nm excitation and the Stoke shifted signal was detected using 595/40 nm band-pass filter. Three different boxes in red, yellow, and green are blown-up and shown alongside for both cELS and TIRF. The yellow box contains the nucleus of the cell. Typically, the nucleus of the cell accommodates a large number of fluorophores. As a result, the fluorescence intensity even in TIRF mode will be high and that can obscure features within the region. But cELS image showed more features in this region because the nucleus is situated slightly above the cell membrane and scattering will be less. However, cELS image shows the presence of coherent scattering, this could be reduced by illuminating the sample from all azimuthal directions as shown in [10, 13]. But the TIRF image exhibited a reduced contrast for the filament like structures which could be attributed to weak fluorescence intensity, non-uniform and unspecific labeling. It can be seen from the images that cELS image generate more uniform and better contrast images as compared to TIRF. In the supplementary material, epi-fluorescence, TIRF and cELS images of the same region of interest presented here is given, see Fig. S7.

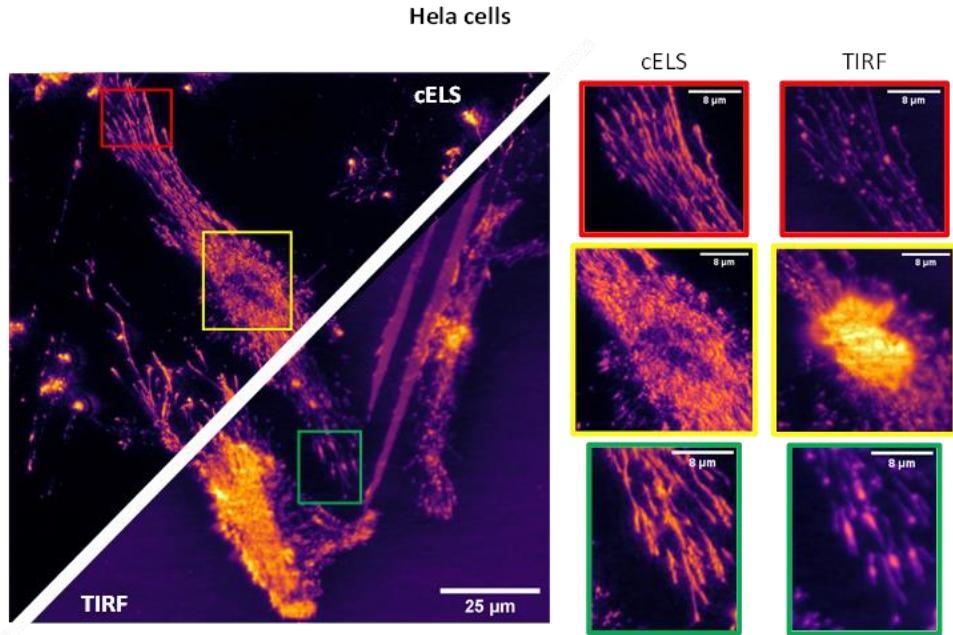


Fig. 5. Comparison between cELS and TIRF images of HeLa cells, scale bar 25 μm . Three different regions of interest enclosed by red, yellow, and green boxes are blown-up and provided alongside. The yellow box shows the nucleus region of the cell whereas the red and green boxes are the filaments, scale bar 8 μm .

4.3 Isotropic resolution enhancement

A multi-moded straight waveguide supports modes predominantly along a straight line. For the waveguide geometry shown in Fig. S1 of supplementary section, the angle the modes make with respect to the optic axis (z-axis) is given by $\theta = \cos^{-1} \beta/kn_1$ [34]. The difference in θ between the first mode ($\beta = 1.75$) and say the twentieth mode ($\beta = 1.76$) is only about 5 degrees. This fact of limited angular diversity between the modes can also be understood from Fig. S2 in supplementary section. It is known that the period of interference fringes is inversely proportional to the angle between the modes. The input to the cosine function in the Eqn. (5) depends on the angle between the two interfering beams. Since the angle between the modes is small, the Fourier peaks of the cosine function are also located close to the origin, which is what is seen experimentally as shown in Fig. S2. To mitigate the abovementioned issues, a four-arm crossing waveguide is proposed (Fig. 6a) and the imaging is performed where several modes from four-arms interference highlighted by the green dotted lines in Fig. 6a. By illuminating the sample from several azimuthal orientations, the illumination frequencies become isotropic [36-38].

The experimental results of 100 nm polystyrene beads are shown in Fig. 6(b) and for this experiment, a four-arm crossing optical waveguide was used as shown in Fig. 6(a). A diffraction-limited image stack of 100 frames acquired is shown in Fig. 6(a). The average diffraction-limited image, cELS image, is shown in Fig. 6(b). MUSICAL is applied to the image stack so acquired and the results are shown alongside. MUSICAL helps resolve beads which remain unresolved in the diffraction-limited image stack. The regions of interest enclosed by yellow, orange and blue boxes are blown-up and shown alongside. The corresponding line profiles, green for cELS and red for MUSICAL on cELS, helps illustrate the fact that the diffraction-limit in label-free mode is circumvented by the proposed cELS methods.

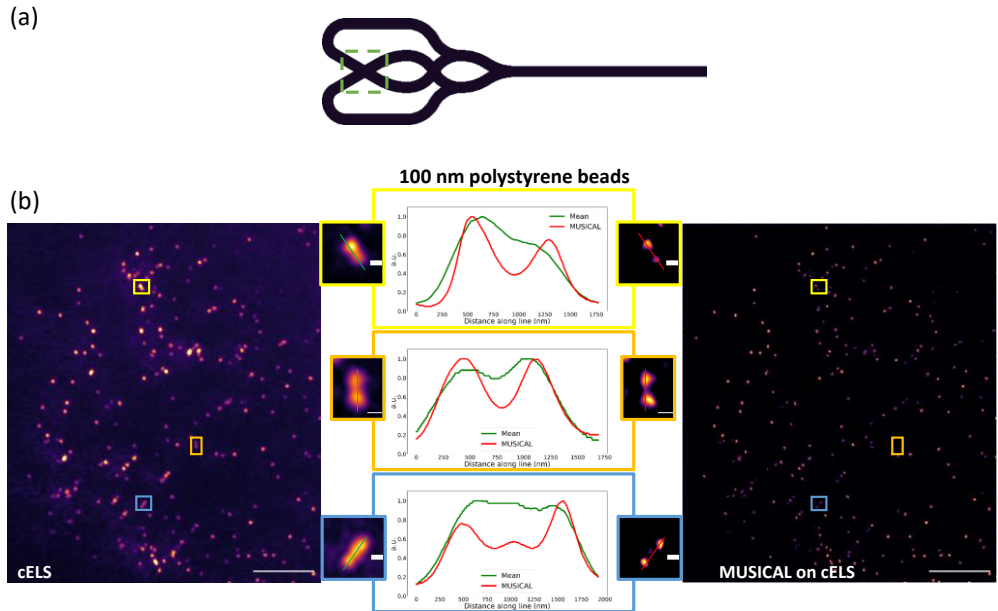


Fig. 6. (a) 4 junction waveguide used for the experiments. The red dotted box in the waveguide shows the imaging region. (b) The mean of 100 images of 100 nm polystyrene beads imaged in cELS mode using a four crossing waveguide is given. A stack of 100 temporally shifted frames is given as the input for MUSICAL. (c) The corresponding MUSICAL reconstruction is shown. Scale bar 10 μ m. Three separate regions of interest in yellow, orange and blue boxes in cELS and the corresponding MUSICAL images are blown up and shown alongside. The line profiles along the dotted lines of the regions given as well. Scale bar 500 nm.

5. Conclusion

In this work we developed the theoretical framework and demonstrate experimental results of label-free superior contrast and super-resolution optical microscopy method using photonic-chip. Although, we obtained promising results in the nascent field of label-free super-resolution optical microscopy, there are still certain unmet challenges. The mixing of high and low spatial frequency components at the image plane due to convolution between the object and illuminating field spectrum as explained earlier, can lead to image distortions. And since the mixing of high frequency signals leads to the generation of moiré patterns which is finally collected by the microscope objective, sub-diffraction limit sized features of the sample will be enlarged more in the image plane [37-38]. All these issues can distort the final image at the camera plane. In this article just as in [11-13, 19], no reconstruction algorithms have been used for image processing. This is a proof-of-concept work involving high index contrast waveguides for label-free superior-contrast imaging by utilizing the multiple modes of the waveguide. However, owing to nanoscale size of samples explored in this work (EVs, nanobead and liposomes), these issues are not significant. Next, for circumventing the diffraction-limit, the partial coherent imaging scheme of cELS employed in tandem with intensity-fluctuation algorithms, may lead to artifacts in the reconstructed image as explained earlier.

Waveguide based imaging is an attractive imaging modality as has been demonstrated by the growing research in this field. Demonstrating label-free superior contrast and super-resolution imaging using waveguide based imaging technology provides an attractive alternative to the nascent field of label-free super-resolution microscopy field. Recently, an affordable waveguide-based 3D printed microscope has been used to image SARS-CoV-2 viroids [39]. Extending this work for label-free imaging of nano-sized viruses, exosomes, EVs and single-cell organisms such as micro-algae and bacteria using cELS would be attractive applications especially when combined with micro-fluidics.

Funding

This project has received funding from the European Union's Horizon 2020 research and innovation program under the Marie Skłodowska-Curie Grant Agreement No. 766181, project "DeLIVER". European Research Council (804233); H2020 Marie Skłodowska-Curie Actions (SEP-210382872); H2020 Marie Skłodowska-Curie Actions (31147, MSCA_ITN: 31147)

Acknowledgements

The authors would like to thank all the staff at UiT for their support during the Covid19 times, Prof. Dr. Ulf Peschel of Friedrich Schiller University Jena and Prof. Dr. Olav Gaute Hellesø for their valuable inputs.

Author contribution

NJ and BSA conceptualized and designed the experiments. FTD designed the waveguide chip and mask for fabrication. NJ, FTD, VD, AA was involved in sample preparation. NJ performed the experiments and analyzed the data. JC and NSB provided the liposome samples. EMG and OS provided the vesicles samples. NJ worked on the theory with inputs from KA and BSA. NJ and BSA wrote the manuscript and all authors commented on the manuscript. KA and BSA supervised the project.

Disclosures

B.S.A. have applied for patent GB1606268.9 for chip-based optical nanoscopy. B.S.A is the co-founder of the company Chip NanoImaging AS, which commercializes on-chip super-resolution microscopy systems.

References

1. Betzig, Eric, and Jay K. Trautman. "Near-field optics: microscopy, spectroscopy, and surface modification beyond the diffraction limit." *Science* 257, no. 5067 (1992): 189-195.
2. Pendry, John Brian. "Negative refraction makes a perfect lens." *Physical review letters* 85, no. 18 (2000): 3966.
3. Fang, Nicholas, Hyesog Lee, Cheng Sun, and Xiang Zhang. "Sub-diffraction-limited optical imaging with a silver superlens." *Science* 308, no. 5721 (2005): 534-537.
4. Liu, Zhaowei, Stéphane Durant, Hyesog Lee, Yuri Pikus, Nicolas Fang, Yi Xiong, Cheng Sun, and Xiang Zhang. "Far-field optical superlens." *Nano letters* 7, no. 2 (2007): 403-408.
5. Durant, Stéphane, Zhaowei Liu, Nicholas Fang, and Xiang Zhang. "Theory of optical imaging beyond the diffraction limit with a far-field superlens." In *Plasmonics: Metallic Nanostructures and Their Optical Properties IV*, vol. 6323, p. 63231H. International Society for Optics and Photonics, 2006.
6. Li, Lin, Wei Guo, Yinzhou Yan, Seoungjun Lee, and Tao Wang. "Label-free super-resolution imaging of adenoviruses by submerged microsphere optical nanoscopy." *Light: Science & Applications* 2, no. 9 (2013): e104-e104.
7. Vellekoop, Ivo M., Aart Lagendijk, and A. P. Mosk. "Exploiting disorder for perfect focusing." *Nature photonics* 4, no. 5 (2010): 320-322.
8. Chen, Gang, Zhong-Quan Wen, and Cheng-Wei Qiu. "Superoscillation: from physics to optical applications." *Light: Science & Applications* 8, no. 1 (2019): 1-23.
9. Berry, Michael Victor, and M. R. Dennis. "Natural superoscillations in monochromatic waves in D dimensions." *Journal of Physics A: Mathematical and Theoretical* 42, no. 2 (2008): 022003.
10. Xu, Xuechu, Xiaowei Liu, Chenlei Pang, Yaoguang Ma, Chao Meng, Jianpei Zhang, Xu Liu, and Qing Yang. "Si3N4 waveguide platform for label-free super-resolution imaging: simulation and analysis." *Journal of Physics D: Applied Physics* 52, no. 28 (2019): 284002.
11. von Olshausen, Philipp, and Alexander Rohrbach. "Coherent total internal reflection dark-field microscopy: label-free imaging beyond the diffraction limit." *Optics letters* 38, no. 20 (2013): 4066-4069.
12. Jünger, Felix, Philipp V. Olshausen, and Alexander Rohrbach. "Fast, label-free super-resolution live-cell imaging using rotating coherent scattering (ROCS) microscopy." *Scientific reports* 6, no. 1 (2016): 1-11.
13. Ruh, Dominic, Julius Mutschler, Moritz Michelbach, and Alexander Rohrbach. "Superior contrast and resolution by image formation in rotating coherent scattering (rocs) microscopy." *Optica* 5, no. 11 (2018): 1371-1381.
14. Helle, Øystein I., David A. Coucheron, Jean-Claude Tinguely, Cristina I. Øie, and Balpreet S. Ahluwalia. "Nanoscopy on-a-chip: super-resolution imaging on the millimeter scale." *Optics express* 27, no. 5 (2019): 6700-6710.
15. Tinguely, Jean-Claude, Øystein Ivar Helle, and Balpreet Singh Ahluwalia. "Silicon nitride waveguide platform for fluorescence microscopy of living cells." *Optics express* 25, no. 22 (2017): 27678-27690.

16. Opstad, Ida S., Florian Ströhl, Marcus Fantham, Colin Hockings, Oliver Vanderpoorten, Francesca W. van Tartwijk, Julie Qiaojin Lin et al. "A waveguide imaging platform for live-cell TIRF imaging of neurons over large fields of view." *Journal of biophotonics* 13, no. 6 (2020): e201960222.
17. Agnarsson, Björn, Asta B. Jónsdóttir, Nina B. Arnfinnsdóttir, and Kristjan Leosson. "On-chip modulation of evanescent illumination and live-cell imaging with polymer waveguides." *Optics express* 19, no. 23 (2011): 22929-22935.
18. Hill, David J., Christopher W. Pinion, Joseph D. Christesen, and James F. Cahoon. "Waveguide scattering microscopy for dark-field imaging and spectroscopy of photonic nanostructures." *AcS Photonics* 1, no. 8 (2014): 725-731.
19. Liu, Xiaowei, Cuifang Kuang, Xiang Hao, Chenlei Pang, Pengfei Xu, Haifeng Li, Ying Liu et al. "Fluorescent nanowire ring illumination for wide-field far-field subdiffraction imaging." *Physical review letters* 118, no. 7 (2017): 076101.
20. Agnarsson, Björn, Anders Lundgren, Anders Gunnarsson, Michael Rabe, Angelika Kunze, Mokhtar Mapar, Lisa Simonsson, Marta Bally, Vladimir P. Zhdanov, and Fredrik Hook. "Evanescent light-scattering microscopy for label-free interfacial imaging: from single sub-100 nm vesicles to live cells." *ACs nano* 9, no. 12 (2015): 11849-11862.
21. Engdahl, Anders Kokkvoll, Stefan Belle, Tung-Cheng Wang, Ralf Hellmann, Thomas Huser, and Mark Schüttelz. "Large Field-of-View Super-Resolution Optical Microscopy Based on Planar Polymer Waveguides." *ACs Photonics* 8, no. 7 (2021): 1944-1950.
22. Helle, Øystein Ivar, Firehun Tsige Dullo, Marcel Lahrberg, Jean-Claude Tinguely, Olav Gaute Hellesø, and Balpreet Singh Ahluwalia. "Structured illumination microscopy using a photonic chip." *Nature Photonics* 14, no. 7 (2020): 431-438.
23. Novotny, Lukas, and Bert Hecht. *Principles of nano-optics*. Cambridge university press, 2012.
24. Diekmann, Robin, Øystein I. Helle, Cristina I. Øie, Peter McCourt, Thomas R. Huser, Mark Schüttelz, and Balpreet S. Ahluwalia. "Chip-based wide field-of-view nanoscopy." *Nature Photonics* 11, no. 5 (2017): 322-328.
25. Jayakumar, Nikhil, Øystein I. Helle, Krishna Agarwal, and Balpreet Singh Ahluwalia. "On-chip TIRF nanoscopy by applying Haar wavelet kernel analysis on intensity fluctuations induced by chip illumination." *Optics Express* 28, no. 24 (2020): 35454-35468.
26. Agarwal, Krishna, and Radek Macháň. "Multiple signal classification algorithm for super-resolution fluorescence microscopy." *Nature communications* 7, no. 1 (2016): 1-9.
27. Opstad, Ida S., Sebastian Acuña, Luís Enrique Villegas Hernandez, Jennifer Cauzzo, Nataša Škalko-Basnet, Balpreet S. Ahluwalia, and Krishna Agarwal. "Fluorescence fluctuations-based super-resolution microscopy techniques: an experimental comparative study." *arXiv preprint arXiv:2008.09195* (2020).
28. Prieve, Dennis C., and John Y. Walz. "Scattering of an evanescent surface wave by a microscopic dielectric sphere." *Applied optics* 32, no. 9 (1993): 1629-1641.
29. Ben-Aryeh, Y. "Tunneling of evanescent waves into propagating waves." *Applied Physics B* 84, no. 1 (2006): 121-124.
30. Kong, Jin Au. "Theory of electromagnetic waves." *New York* (1975).
31. Wolf, Emil. *Introduction to the Theory of Coherence and Polarization of Light*. Cambridge University Press, 2007.
32. Goodman, Joseph W. *Statistical optics*. John Wiley & Sons, 2015.
33. Cauzzo, Jennifer, Nikhil Jayakumar, Balpreet Singh Ahluwalia, Azeem Ahmad, and Nataša Škalko-Basnet. "Characterization of Liposomes Using Quantitative Phase Microscopy (QPM)." *Pharmaceutics* 13, no. 5 (2021): 590.
34. Ajoy Ghatak and K. Thyagarajan. *An introduction to fiber optics*. Cambridge university press, 1998.
35. Ströhl, Florian, Ida S. Opstad, Jean-Claude Tinguely, Firehun T. Dullo, Ioanna Mela, Johannes WM Osterrieth, Balpreet S. Ahluwalia, and Clemens F. Kaminski. "Super-condenser enables label-free nanoscopy." *Optics express* 27, no. 18 (2019): 25280-25292.
36. Pang, Chenlei, Jingxi Li, Mingwei Tang, Jianpu Wang, Ioanna Mela, Florian Ströhl, Lisa Hecker et al. "On-Chip Super-Resolution Imaging with Fluorescent Polymer Films." *Advanced Functional Materials* 29, no. 27 (2019): 1900126.
37. Tang, Mingwei, Xiaowei Liu, Zhong Wen, Feihong Lin, Chao Meng, Xu Liu, Yaoguang Ma, and Qing Yang. "Far-Field Superresolution Imaging via Spatial Frequency Modulation." *Laser & Photonics Reviews* 14, no. 11 (2020): 1900011.
38. Hao, Xiang, Cuifang Kuang, Yanghui Li, and Xu Liu. "Evanescent-wave-induced frequency shift for optical superresolution imaging." *Optics letters* 38, no. 14 (2013): 2455-2458.
39. Diederich, Benedict, Øystein Helle, Patrick Then, Pablo Carravilla, Kay O. Schink, Franziska Hornung, Stefanie Deinhardt-Emmer, Christian Eggeling, Balpreet Singh Ahluwalia, and Rainer Heintzmann. "Nanoscopy on the Chea (i) p." (2020).

Label-free chip-based evanescent light scattering super-resolution and superior-contrast optical microscopy (cELS)

NIKHIL JAYAKUMAR,^{1,6} FIREHUN T DULLO,² VISHESH DUBEY,¹ AZEEM AHMAD,¹ JENNIFER CAUZZO,³ EDUARDA MAZAGAO GUERREIRO,⁴ OMRI SNIR,⁴ NATASA SKALKO-BASNET,³ KRISHNA AGARWAL,¹ AND BALPREET SINGH AHLUWALIA^{1,5,7}

¹ Department of Physics and Technology, UiT The Arctic University of Norway, Tromsø 9037, Norway

² SINTEF Digital, Department of Microsystems and Nanotechnology, Gaustadalleen 23C, 0373 Oslo, Norway

³ Department of Pharmacy, Faculty of Health Sciences, UiT The Arctic University of Norway, Tromsø 9037, Norway

⁴ Department of Clinical Medicine, UiT The Arctic University of Norway, Tromsø 9037, Norway

⁵ Department of Clinical Science, Intervention and Technology, Karolinska Institute, 17177 Stockholm, Sweden

⁶nik.jay.hil@gmail.com, ⁷balpreet.singh.ahluwalia@uit.no

This document supplements the work described in the main article. The concept of modes, the theory behind the formation of images in cELS and the application of cELS to imaging is provided here.

S1. Optical modes in waveguides

Waveguide core material	Refractive index at 660 nm
Si_3N_4	2.0804
Ta_2O_5	2.2080
TiO_2	2.5607

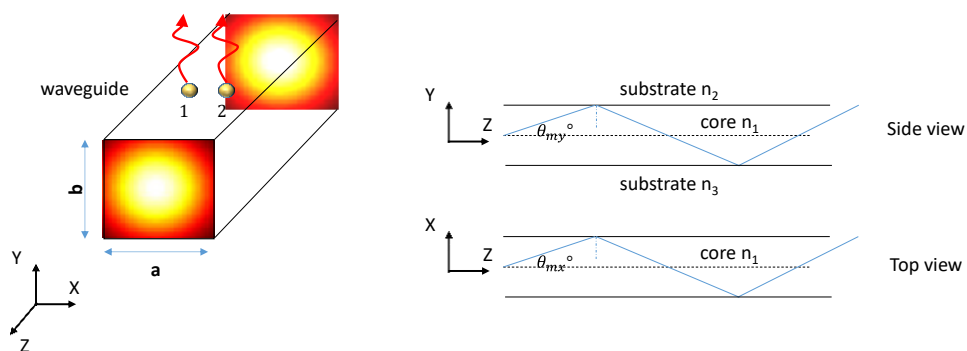


Fig. S1. Schematic of a rectangular waveguide with a Gaussian mode profile being guided along its length. The modes are field distributions that propagate keeping its transverse profile (x-y) intact. They merely accumulate a phase with distance 'z'. A waveguide supports discrete and not a continuum set of modes, ψ_m , and each mode is characterized by a discrete angle of propagation θ_m . Two-point particles, placed on the x-z plane, with a different refractive index scatters the evanescent field into the far-field.

Assume that the dielectric constant ' ϵ ' depends only on the transverse co-ordinate, x and y. It means that along z-axis, the modes will accumulate only a phase as it propagates along

the length of the waveguide. This will help reduce Maxwell's equations to two independent sets of solutions called transverse electric (TE) and transverse magnetic modes. For TE modes the Helmholtz equation is given as

$$\left(\frac{d^2}{dx^2} + \frac{d^2}{dy^2}\right)E_y + k_0^2 \epsilon(x, y) E_y = \beta^2 E_y \quad (S1)$$

where E_y is the y-component of the electric field, $k_0 = \omega/c$ is the free-space wave number and β is the propagation constant of the mode. For comparison, the two-dimensional time-independent Schroedinger equation is given, where $V(x, y)$ is the potential, $\psi_{(x,y)}$ is the wavefunction and E is the energy of the particle.

$$\frac{-\hbar^2}{2m} \left(\frac{d^2}{dx^2} + \frac{d^2}{dy^2}\right)\psi_{(x,y)} + V(x, y)\psi_{(x,y)} = E\psi_{(x,y)} \quad (S2)$$

For the waveguides used here the refractive index of the core n_1 is greater than that of the substrates. Now comparing Eqn. (S1) and (S2), it can be seen that the dielectric constant is similar to the potential function. Or it means that light gets attracted to areas of higher dielectric constant, i.e., light gets attracted towards the core for the waveguides considered here. The solution of Eqn. (S1) can be found to be oscillatory in nature inside the core and the boundary conditions at the core-cladding interface impose decaying behavior for the evanescent fields. Now for a rectangular dielectric waveguide with dielectric constant $\epsilon(x, y)$ the general Helmholtz equation when solved yields the following solutions.

$$\begin{aligned} E_x &\approx \cos \frac{m\pi x}{a} \sin \frac{n\pi y}{b} e^{-i\beta z} \\ E_y &\approx \sin \frac{m\pi x}{a} \cos \frac{n\pi y}{b} e^{-i\beta z} \\ H_x &\approx \sin \frac{m\pi x}{a} \cos \frac{n\pi y}{b} e^{-i\beta z} \\ H_y &\approx \cos \frac{m\pi x}{a} \sin \frac{n\pi y}{b} e^{-i\beta z} \end{aligned} \quad (S3)$$

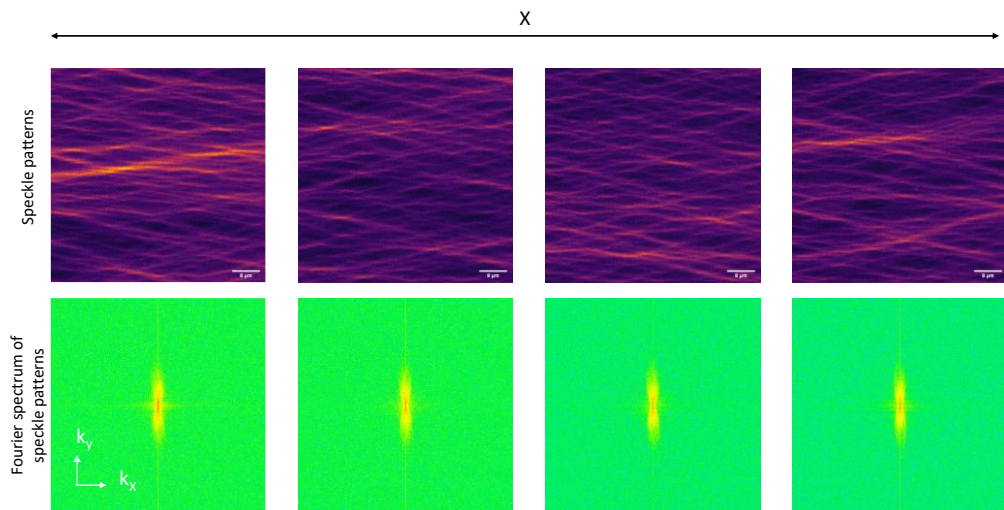


Fig. S2. The multiple modes overlap in straight waveguides leading to speckles. The use of straight waveguides limits the illumination spatial frequencies to regions around the vertical axis. This is demonstrated by the Fourier spectrum of the illumination frequencies. Scale bar 8 μm .

The above equation constitutes the TE_{mn} modes where $m = 0, 1, 2, \dots$ and $n = 0, 1, 2, \dots$. It implies that there are discrete and not a continuum of modes. Each of these mode can be also be represented as a sum of two plane waves propagating at angles $\pm\theta$ with respect to the z-axis as shown in Fig. S1. These modes are sustained along the length of the waveguide through the generation of evanescent waves at the core-cladding interface. The physical understanding of the generation of evanescent waves can be as follows. The incident wave vector $\vec{k}_i = \alpha_i \hat{x} + \beta_i \hat{y} + \gamma_i \hat{z}$ strikes the core-substrate interface as shown in Fig. S1. The dispersion relation for the wave vector in the core is given by $\vec{k}_i^2 = \alpha_i^2 + \beta_i^2 + \gamma_i^2$ and for the cladding is $\vec{k}_{cla}^2 = \alpha_{cla}^2 + \beta_{cla}^2 + \gamma_{cla}^2$. The high index core squeezes the wave fronts at the interface. This implies that for phase matching at the core-cladding interface one of the wave vector components, β_{cla} , of the cladding has to become imaginary. This imaginary component of the wave vector leads to an exponential decay of the field away from the interface, i.e., along the y-axis in Fig. S1, and they are known as evanescent waves.

The discrete number of modes imply that there are discrete angles of propagation, and they can overlap in space and lead to speckles or multi-mode interference patterns as shown in Fig. S2. This makes the illumination profile non-uniform and speckle ridden. The Fourier spectrum of the illumination profile shows that this restricts the illumination spatial frequencies along the k_y axis. As a result, isotropic resolution enhancement is not possible. Also when intensity fluctuation based algorithms are applied on image stacks acquired using straight waveguides, the fluctuations in intensity will be predominantly along the vertical axis and thereby, restricting the resolution enhancement to the vertical axis.

S2. Theory of image formation in cELS

Consider two particles ‘1’ and ‘2’ placed on top of the waveguide surface as shown in Fig. S3. The input coherent laser light excites a few modes inside the waveguide. For clarity only two of these modes are depicted in Fig. S3. As mentioned in Ref. [1], any mode ‘m’ may be decomposed into a pair of plane waves propagating at angle $\pm\theta_m$ with respect to the z-axis. Therefore, two modes are represented in green (mode m1) and red color (mode m2) propagating inside the core. The tails of these modes extend into the cladding and interact with the particles located there. The particles are polarized as a result and radiate into the far-field which is detected by the camera.

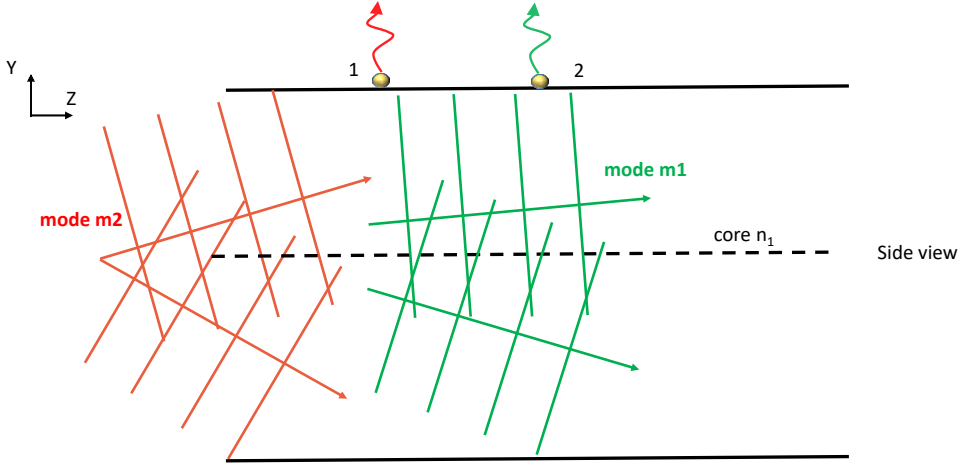


Fig. S3. Theory of cELS image formation. Two modes of the waveguide m1 and m2 are shown in green and red color respectively. The modes are decomposed into a pair of plane waves propagating at discrete angles with respect to the optical axis along z. The evanescent tails of these guided modes interact with particles 1 and 2 placed on the surface and as a result, light is scattered into the far-field.

Neglecting the vectorial aspect of light, let the scalar field generated by the two particles be $U_1(\mathbf{r}, t) = a_1(\mathbf{r})e^{i\varphi_1(\mathbf{r}, t) - i\omega t}$ and $U_2(\mathbf{r}, t) = a_2(\mathbf{r})e^{i\varphi_2(\mathbf{r}, t) - i\omega t}$. For simplicity assume that the two particles are identical and radiate with the same amplitude distribution, i.e., $a_1(\mathbf{r}) = a_2(\mathbf{r}) = a(\mathbf{r})$. The coherence lengths of waveguides have been experimentally calculated in Ref. [2] via the visibility of interference fringes. For silicon waveguides fabricated in standard CMOS foundry, the coherence lengths are found to be approximately 4.17 mm for rib and 1.6 mm for strip geometry [2] and it is about 27 m for phosphorous-doped core silica on silicon waveguides. The main source of fluctuations is attributed to variations in waveguide dimension and composition. These fluctuations manifest mainly in the phase of the light scattered by the particles and is accounted for by making the phase, $\varphi_j(\mathbf{r}) = \vec{k}_j \cdot \vec{r}$, a function of time 't', i.e., $\varphi_j(\mathbf{r}) = \varphi_j(\mathbf{r}, t)$, where $j=1,2$ represent the two particles described here. The total electric field $U_T(\mathbf{r}, t)$ reaching the camera will be

$$U_T(\mathbf{r}, t) = (U_1(\mathbf{r}, t) + U_2(\mathbf{r}, t)) \otimes h(\mathbf{r}) \quad (\text{S4})$$

where $h(\mathbf{r})$ is the coherent transfer function of the optical system, \otimes represents convolution operation and bold letters represent vectors. The spectrum of the total field reaching the camera may be computed as

$$\widetilde{U}_T(\mathbf{k}, t) = \widetilde{U}_1(\mathbf{k}, t)\widetilde{H}(\mathbf{k}) + \widetilde{U}_2(\mathbf{k}, t)\widetilde{H}(\mathbf{k}) \quad (\text{S5})$$

where $\widetilde{U}_j(\mathbf{k}, t)$ is the Fourier transform of the amplitudes of the particles and $\widetilde{H}(\mathbf{k})$ is the amplitude transfer function. The Fourier transform of the fields $U_1(\mathbf{r}, t)$ and $U_2(\mathbf{r}, t)$ may be computed as $\widetilde{U}_1(\mathbf{k}, t) = \tilde{A}(\mathbf{k}) \otimes \delta(\mathbf{k} - \mathbf{k}_1) = \tilde{A}(\mathbf{k}_1)$ and $\widetilde{U}_2(\mathbf{k}, t) = \tilde{A}(\mathbf{k}) \otimes \delta(\mathbf{k} - \mathbf{k}_2) = \tilde{A}(\mathbf{k}_2)$. Substituting this result into Eqn. (S5) we can see that the shifted object spectrum field is low passed by the coherent transfer function. Now the instantaneous intensity in real space can be computed from Eqn. (S4) as follows

$$I_T(\mathbf{r}, t) = [(U_1(\mathbf{r}, t) + U_2(\mathbf{r}, t)) \otimes h(\mathbf{r})] \cdot [(U_1^*(\mathbf{r}, t) + U_2^*(\mathbf{r}, t)) \otimes h^*(\mathbf{r})] \quad (\text{S6})$$

In this work, we scanned the input facet of the waveguide with a galvo to generate different sets of guided mode inside the waveguide. This generates speckle patterns that get added up incoherently during the integration time of the camera at the detector plane. This can be represented mathematically as

$$\langle I_T(\mathbf{r}, t) \rangle = I_1(\mathbf{r}, t) + I_2(\mathbf{r}, t) + \dots = \sum_n I_n(\mathbf{r}, t) \quad (S7)$$

The final image generated by the camera is obtained as described by Eqn. (S7). To understand the Fourier transform of the cELS image generated, Eqn. (S6) may be Fourier transformed and then generalized for Eqn. (S7). Fourier transforming Eqn. (S6) gives

$$\tilde{I}_T(\mathbf{k}, t) = [(\tilde{U}_1(\mathbf{k}, t) + \tilde{U}_2(\mathbf{k}, t)).\tilde{H}(\mathbf{k})] \otimes [(\tilde{U}_1^*(\mathbf{k}, t) + \tilde{U}_2^*(\mathbf{k}, t)).\tilde{H}^*(\mathbf{k})] \quad (S8)$$

Substituting for $U_j(\mathbf{r}, t)$ in Eqn. (S8), it can be further reduced to the following form.

$$\tilde{I}_T(\mathbf{k}, t) = [\tilde{A}(\mathbf{k}_1).\tilde{H}(\mathbf{k}) + \tilde{A}(\mathbf{k}_2).\tilde{H}(\mathbf{k})] \otimes [\tilde{A}^*(\mathbf{k}_1).\tilde{H}^*(\mathbf{k}) + \tilde{A}^*(\mathbf{k}_2).\tilde{H}^*(\mathbf{k})] \quad (S9)$$

where $\tilde{A}(\mathbf{k}_1)$ and $\tilde{A}(\mathbf{k}_2)$ represent the shifted Fourier spectrum of the two particles corresponding to the illumination fields exciting them, $\tilde{H}(\mathbf{k})$ is the Fourier transform of the coherent transfer function and possess Hermitian symmetry, $\tilde{H}(-\mathbf{k}) = \tilde{H}^*(\mathbf{k})$. The spectrum of the final image obtained will then be given by adding the spectra described by Eqn. (S9). For ease of notation let $\tilde{P}(\mathbf{k}) = \tilde{A}(\mathbf{k}_1).\tilde{H}(\mathbf{k})$ and $\tilde{Q}(\mathbf{k}) = \tilde{A}(\mathbf{k}_2).\tilde{H}(\mathbf{k})$. Then Eqn. (S9) can be rewritten as

$$\tilde{I}_T(\mathbf{k}, t) = \tilde{P}(\mathbf{k}) \otimes \tilde{P}^*(\mathbf{k}) + \tilde{Q}(\mathbf{k}) \otimes \tilde{Q}^*(\mathbf{k}) + \tilde{P}(\mathbf{k}) \otimes \tilde{Q}^*(\mathbf{k}) + \tilde{P}^*(\mathbf{k}) \otimes \tilde{Q}(\mathbf{k}) \quad (S10)$$

For incoherent illumination the cross-terms in the above-mentioned equation, $\tilde{P}(\mathbf{k}) \otimes \tilde{Q}^*(\mathbf{k})$ and $\tilde{P}^*(\mathbf{k}) \otimes \tilde{Q}(\mathbf{k})$, will tend to zero on time averaging and therefore, becomes linear in intensity. Thus, Eqn. (S10) represents the spectrum for coherent illumination. The spectrum of the final image will be the sum of many individual spectrums represented by Eqn. (S10) as explained earlier.

The following interesting cases may be noted while illuminating with waveguide modes. As per first order Born approximation, the incident and scattered waves can be assumed to have the same phase [3]. Therefore, the phase difference between the scattered waves off the two particles can be assumed to be dependent only on the illuminating field, the phase of which varies with the position of the particles. This can be understood as follows. Consider the situation where the two particles depicted as in Fig. (S3) are illuminated by the same mode. The two particles are assumed to be located at a separation of Rayleigh distance = $0.61\lambda/NA$, where NA is the numerical aperture of the microscope objective and λ is the wavelength of detected light. In the experiments presented here, $\lambda = 660$ nm and NA = 1.2. Therefore, the two particles can be assumed to be located along the x-axis at (0, b/2, 0) and (0.508a, b/2, 0). In case of incoherent illumination, i.e., if fluorescent particles are used, they will be just resolved as per Rayleigh's resolution criteria. However, in case of cELS the following cases may arise.

1. The two particles are illuminated by the same mode m1, see Fig. (S3). For example consider illumination with TE₁₁ mode (m=1, n=1). Substituting the particle's location into Eqn. (S3) it can be seen that the phase difference between the scattered light reaching the detector will be approximately 1.6 radians. It implies that the interference term will not cause as much dip in intensity as observed in Rayleigh resolution limit, which corresponds to a phase difference of π radians between the particles. It may be noted that the field equations given in Eqn. (S3) are the oscillatory solutions for the guided modes inside the core. For evanescent waves the same field distribution is obtained except for the fact that γ_i becomes complex, i.e., exponentially decaying along the z-axis.
2. The two particles are illuminated by say TE₁₁ and TE₂₁ mode. Then the phase difference between the particles. From Eqn. (S3), is found to be π radians which

corresponds to the particles being resolved as per Rayleigh's criteria. Hence, a much deeper dip in intensity is observed than in the previous case.

Within the exposure time of the camera, the galvo would have oscillated several times back and forth. In the experiments presented here the galvo oscillation rate is set as a prime number at 1013 Hz. The exposure time of the camera was typically set to 30 ms. It means that the galvo would have oscillated approximately 30 times back and forth within 30 ms. The phase of the light varies at a rate orders of magnitude higher than the exposure time of the camera or the oscillation rate of the galvo. At each position of the galvo, it will excite a set of modes. The particles scatter the light that interferes at the camera plane. The galvo then moves to the next position and again the particles scatter light with a different phase difference between them as explained earlier. The final image generated by the camera at the end of its integration time will be the sum of the different intensity distributions of the light scattered by particles. The phase difference between light scattered off by the particles due to multi-mode illumination can be assumed to have values ranging between $-\pi$ and $+\pi$ radians. Therefore, the final image formed at the camera plane can be considered a superposition of different speckle patterns with different phase differences, and thus resembling a random walk. This helps mitigate speckle noise as illustrated in [4].

S3. Role of coherence in image formation

The longitudinal coherence lengths of a light source may be deduced from Wiener-Khintchin theorem and is given by [5]:

$$\frac{1}{L_c} \approx \frac{2 \sin^2 \theta/2}{\lambda_0} + \frac{\Delta\lambda}{\lambda_0^2} \cos^2 \theta/2 \quad (\text{S10})$$

where L_c is the longitudinal coherence length as a function of both angular and temporal spectrum, λ_0 is the center wavelength of the temporal spectrum of a source with temporal bandwidth $\Delta\lambda$, $l_c \approx \frac{\lambda_0^2}{\Delta\lambda}$ is the temporal coherence length of the light source and θ is width of angular spectrum. The longitudinal coherence length gives the length over which the photons remain correlated. A similar expression as in Eqn. (S10) is also obtained for transverse coherence lengths [5]. The coherence volume of the field may be defined as the product of the transversal and longitudinal coherence lengths. Only photons within the coherence volume can interfere to generate a sustained interference pattern.

For the experiments presented in this article, cELS imaging have been carried out using a diode laser, Cobalt Flamenco 660 nm laser. The bandwidth of this laser is < 1 GHz as mentioned in the company website. This implies a coherence time of ≈ 159 ns. The exposure time of the camera is 30 ms and therefore, a number of different speckle patterns as described earlier will get generated within the integration time of the camera. As a result,

the degree of coherence is not unity and therefore, through the use of this laser itself some mitigation in speckle noise is achieved. In contrast, if fluorescence imaging is performed, for example such as TIRF mentioned in this article, a larger number of speckle patterns will get generated within the integration time of the camera. It means the use of fluorescence will yield a highly incoherent illumination. For example, if the bandwidth of fluorescence emission is 100 nm, then the coherence time of the laser can be shown to ≈ 3 fs. It means that more than 10^6 speckle patterns as compared to cELS imaging will get generated within the exposure time of the camera and therefore, more reduction in speckle noise is observed.

S4. Waveguide fabrication and characterization

The imaging platform is based on silicon nitride (Si_3N_4) waveguides on a silicon wafer, fabricated by low-pressure chemical vapor deposition and reactive-ion etching as detailed in [6]. Waveguide chips were produced at the Institute of Microelectronics Barcelona (IMB-CNM, Spain). Waveguide fabrication steps as follows: a 2 μm thick silica layer was grown thermally on the silicon wafer, followed by deposition of silicon nitride layer via low-pressure chemical vapor deposition (LPCVD) at 800°C. The waveguide structures are then created via photolithography and reactive ion etching (RIE) to produce the required 2-D waveguides.

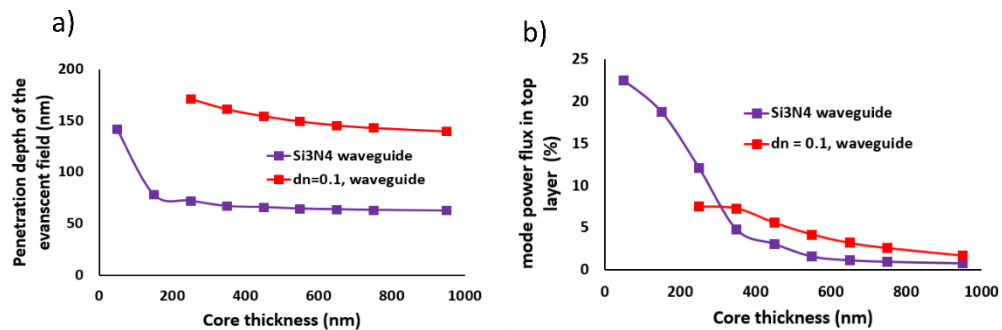


Fig. S4. The (a) penetration depth and (b) field intensity of a TE1 mode of Si_3N_4 high index core ($\Delta n \approx 0.5$) waveguide and an index matched waveguide ($\Delta n \approx 0.1$) are provided here.

S5. Liposomes preparation, characterization and labeling

Labeled liposomes were formulated with a mass ratio 100:1 comprising soy phosphatidylcholine (SPC, Lipoid S100, main lipid ingredient kindly provided by Lipoid GmbH, Ludwigshafen, Germany) and 1-myristoyl-2-{6-[(7-nitro-2-1,3-benzoxadiazol-4-yl)amino]hexanoyl}-sn-glycero-3- phosphocholine (fluorescently labeled phospholipid, obtained from Avanti Polar Lipids, Alabaster, AL, USA). The film hydration method was used to prepare a multilamellar/multivesicular dispersion. A methanol solution of both ingredients was subjected to gentle solvent removal (Büchi Rotavapor, Büchi

Labortechnik, Flawil, Switzerland) and the thin film obtained was rehydrated by hand shaking to the final concentration of 10 mg/mL of SPC and 0.1 mg/mL of labeled lipid. Stepwise extrusion through polycarbonate membranes (Nucleopore®) of 800, 400 and 200 nm sieving sizes was performed for efficient size reduction of the vesicles. [Citation: our paper] Hence, dynamic light scattering was utilized for conventional characterization (Malvern Zetasizer Nano – SZ, Malvern Oxford, UK), obtaining Gaussian distributions for size (121 ± 30 nm, with polydispersity index of 0.19 ± 0.01) and zeta-potential (-9.39 ± 3.3 mV, as estimation of the surface charge) [7].

S6. EV preparation, characterization and labeling

Isolation of platelet-derived extracellular vesicles

Blood (50 ml) was collected from healthy volunteers into non-glass Vacutte tubes (6ml Z with no additive, Greiner Bio-One, Austria). Acidic citrate dextrose (ACD, 39 mM citric acid, 75 mM sodium citrate, 135 mM [D]-glucose, pH 4.5) buffer was added immediately to the tubes to prevent clotting. Platelet rich plasma (PRP) was generated by centrifuging the blood at 140gx for 15 min with no brakes. PRP was transferred to fresh tubes and ACD and 2.83 μ M Prostaglandin E1 (PGE1, Sigma) were added and centrifuged at 900 gx for 15 min to pellet the platelets. Supernatant was discarded and platelets were resuspended in Ca^{2+} free Tyrode-HEPES buffer (137 mM NaCl, 0.3 mM NaH_2PO_4 , 3.5 mM HEPES, 5.5 mM [D]-glucose, pH 7.35) and washed twice by centrifuging at 900 gx for 15 min. Platelet washes were carried out in the presence of PGE1 at 2.83 μ M to prevent their activation. Once washed, platelets were resuspended in Tyrode buffer (137 mM NaCl, 0.3 mM NaH_2PO_4 , 3.5 mM HEPES, 5.5 mM [D]-glucose, 1 mM MgCl_2 , 2 mM CaCl_2 , 3 mM KCl, pH 7.35) to a final concentration of 250×10^6 platelets/ml. Platelets were stimulated with 20 mM thrombin receptor activator peptide 6 (TRAP6, Sigma) for 15 min at 37 °C with and EDTA 20 mM was added to stop the reactions. To remove platelets, samples were centrifuged at 2,500 gx for 15 min and platelet-free supernatants were collected and stored at -80 °C until use. To purify EVs, supernatants were thawed and centrifuged at 20,000 gx for 30 min at 4 °C. EV pellets were resuspended in 0.1V of particle free Dulbecco's Phosphate-buffered saline (DPBS, Sigma) and stained with 100 μ l FITC-conjugated lactadherin (1.6 μ M, Haematological Technologies). Importantly, to avoid sample contamination, FITC-conjugated lactadherin was pre-filtered using an Ultrafree MC-GV filter (Merck Millipore, Ireland). Extracellular vesicles were incubated with FITC-conjugated lactadherin for 15 min on ice, in the dark. Excess stain was washed by centrifuging at 20,000 gx for 30 min, 4 °C. Supernatants were discarded and extracellular vesicles were resuspended in 120 μ l particle free DPBS, and filtered in a Ultrafree MC-GV filter at 5,000 gx for 30 sec. The study of extracellular vesicles was approved by the regional committee for medical and health research ethics (REC North) and donors have signed an informed consent.

S7. HeLa cell labeling

HeLa cells were grown in the culture media prepared in minimum essential medium (MEM) supplemented with 10% fetal bovine serum and 1% penicillin/streptomycin. The cells were seeded into the PDMS well chambers located on waveguide chip and kept in a standard humidified incubator at 37°C with 5% CO₂ overnight. For live-cell imaging, the culture medium was aspirated and replaced with pre-warmed Live Cell Imaging Solution (Invitrogen) before imaging. For actin labeling, HeLa cells were fixed for ~15 minutes using 4% paraformaldehyde in PBS. Cells were then washed in PBS followed by incubation with 0.1% Triton X-100 in PBS for 10 minutes. The cells were further washed

3 times in PBS for a few minutes each time. Cells were then incubated with Atto-565 phalloidin (1:50 for in PBS for 90 minutes.

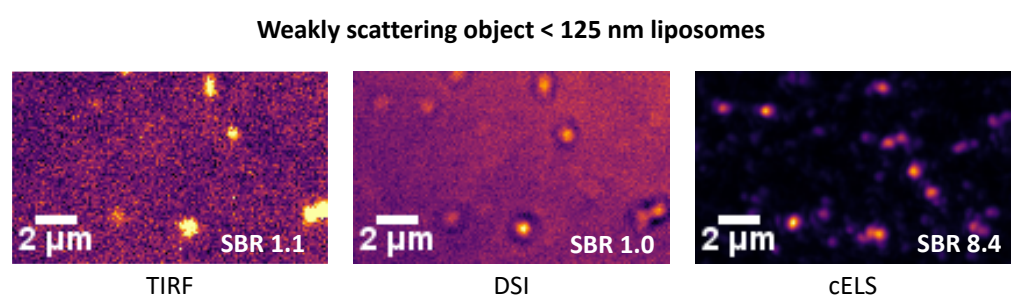


Fig. S5. TIRF, DSI and cELS images of < 125 nm liposomes. The signal to background ratio is also given as inset in the figure. cELS shows the presence of larger number of scattering particles as opposed to the other methods of illumination. Scale bar 2 μ m.

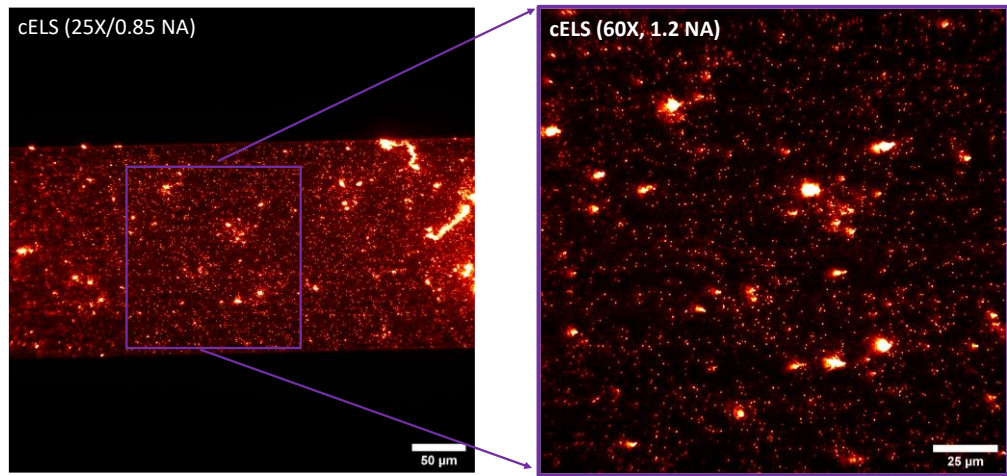


Fig. S6. Scalable field-of-view using cELS. Decoupling of illumination and detection paths enable scalable field-of-view as illustrated here. A larger field-of-view (shown on left) of 100 nm polystyrene beads is imaged using a 25X/0.85 NA microscope objective initially and then for higher resolution, a smaller field-of-view is imaged using a 60X/1.2 NA microscope objective.

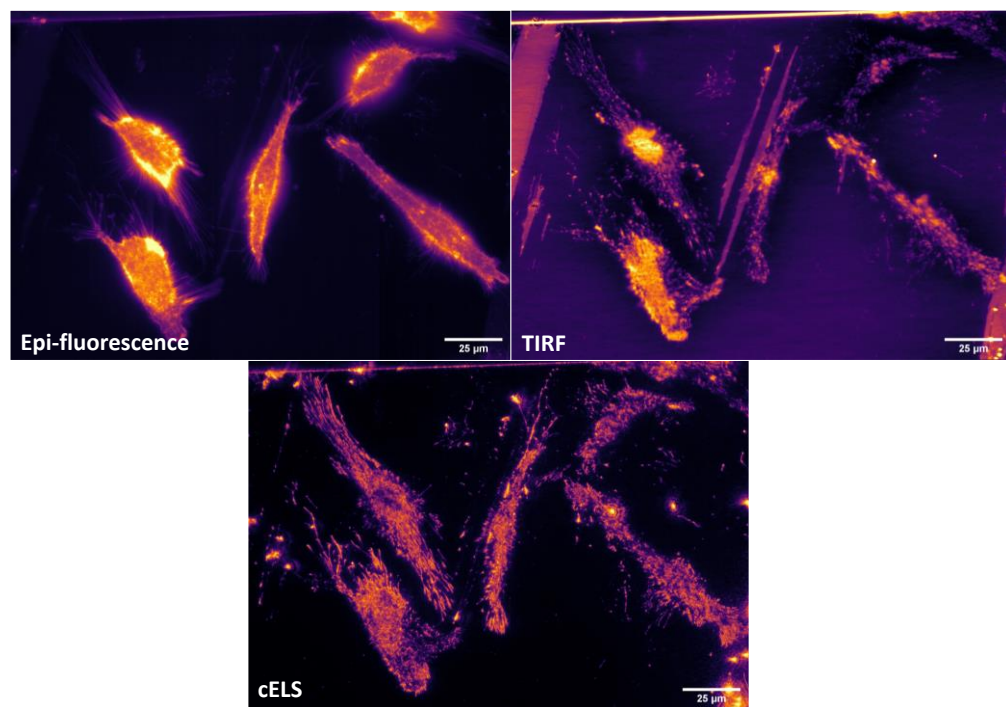


Fig. S7. Comparison between epi-fluorescence, TIRF and cELS images of Hela cells with the same field-of-view.
Scale bar 25 μ m.

Figure	Sample under study	Experiment	Excitation λ	Detection λ	Exposure time	Filters used (LP –long	Additional comments
--------	--------------------	------------	----------------------	---------------------	---------------	------------------------	---------------------

						pass, BP – band pass)	
3(a)	60 nm polystyrene beads	cELS	660 nm	660 nm	30 ms	-	
		TIRF	532 nm	595 nm	50 ms	532 nm LP 595/40 nm BP	
3(b-e)	< 125 nm liposomes	Epi-illumination laser	660 nm	660 nm	30 ms	-	
		TIRF	488 nm	520 nm	200 ms	488 nm LP 520/35 nm BP	
		Epi-illumination spatially incoherent	660 nm	660 nm	30 ms	-	
		cELS	660 nm	660 nm	30 ms	-	
3(f)	< 225 nm extra- cellular vesicles	TIRF	488 nm	520 nm	100 ms	488 nm LP 520/35 nm BP	
		cELS	660 nm	660 nm	30 ms	-	
4	100 nm polystyrene beads	20X/0.45 NA (cELS, DSI, WL)	660 nm	660 nm	30 ms	-	
5	Fixed Hela cells	cELS	660 nm	660 nm	50 ms	-	
		TIRF	532 nm	595 nm	50 ms	532 nm LP 595/40 nm BP	

6(b)	100 nm polystyrene beads	cELS/MUSICAL	660 nm	660 nm	30 ms	-	Stack of 100 images acquired in cELS mode used as input for MUSICAL. Threshold value for MUSICAL set at -0.8 and subpixelation at 10.
------	--------------------------	--------------	--------	--------	-------	---	---------------------------------------------------------------------------------------------------------------------------------------

Table 1: Particulars of the experiments detailed in the main article.

References

1. Ajoy Ghatak and K. Thyagarajan. *An introduction to fiber optics*. Cambridge university press, 1998.
2. Yang, Yisu, Yangjin Ma, Hang Guan, Yang Liu, Steven Danziger, Stewart Ocheltree, Keren Bergman, Tom Baehr-Jones, and Michael Hochberg. "Phase coherence length in silicon photonic platform." *Optics express* 23, no. 13 (2015): 16890-16902.
3. Blugel, Stefan. "A 2 Scattering Theory: Born Series." (2012).
4. Goodman, Joseph W. *Statistical optics*. John Wiley & Sons, 2015.
5. Ryabukho, V. P., D. V. Lyakin, A. A. Grebenyuk, and S. S. Klykov. "Wiener–Khintchin theorem for spatial coherence of optical wave field." *Journal of Optics* 15, no. 2 (2013): 025405.
6. F. Prieto, B. Sepúlveda, A. Calle, A. Llobera, C. Domínguez, A. Abad, A. Montoya, and L. M. Lechuga, "An integrated optical interferometric nanodevice based on silicon technology for biosensor applications." *Nanotechnology* 14, 907 (2003).
7. Cauzzo, Jennifer, Nikhil Jayakumar, Balpreet Singh Ahluwalia, Azeem Ahmad, and Nataša Škalko-Basnet. "Characterization of Liposomes Using Quantitative Phase Microscopy (QPM)." *Pharmaceutics* 13, no. 5 (2021): 590.